Research Article Vol. 31, No. 2 / 16 Jan 2023 / Optics Express 2710
Optics EXPRESS

Entanglement mediated by DC current induced nonreciprocal graphene plasmonics

JAY A. BERRES,[1,4,*] S. ALI HASSANI GANGARAJ,[2,3] AND GEORGE W. HANSON[1]

[1]Department of Electrical Engineering, University of Wisconsin-Milwaukee, Milwaukee, Wisconsin 53211, USA
[2]Department of Electrical and Computer Engineering, University of Wisconsin-Madison, Madison, Wisconsin 53706, USA
[3]Science and Technology Division, Corning Incorporated, Sullivan Park, Corning, NY 14831, USA
[4]jaberres@uwm.edu
[*]jaberres@gmail.com

Abstract: We investigate entanglement mediated by DC current induced nonreciprocal graphene plasmon polaritons. Nonreciprocal systems are ideal for the enhancement, control, and preservation of entanglement due to the potential for unidirectional beam-like wave propagation, i.e., efficiently transporting photons from one emitter to another. Using a quantum master equation and three-dimensional Green's function analysis, we investigate a system consisting of two two-level emitters dominantly interacting via electric current induced nonreciprocal plasmonic modes of a graphene waveguide. We use concurrence as a measure of entanglement. We show that nonreciprocal graphene plasmon polaritons are a promising candidate to generate and mediate concurrence, where it is shown that there is good enhancement and control of entanglement over vacuum, which is beneficial for the broad applications of entanglement as a quantum resource. We believe our findings contribute to the development of quantum devices, enabling efficient and tunable entanglement between two-level systems, which is a central goal in quantum technologies.

1. Introduction

The key element of any quantum system, e.g., a two-level system, is for the quantum emitters to interact with the environment, and exchange photons with other neighbor emitters. Tailoring these interactions fundamentally alters the performance of quantum devices for maintaining entanglement and quantum superposition between two separated quantum emitters. Recent work has investigated entanglement mediated by surface plasmon polaritons (SPPs) by means of various media and plasmonic waveguide structures, e.g., V-shaped waveguides cut in a flat metal plane [1–3] and photonic topological insulators (PTIs) [4–8]. It was shown that entanglement mediation could be enhanced, controlled, and even preserved in the presence of large structural defects (by means of the PTIs) by SPPs in the various plasmonic environments. Additionally, in a recent work [9], a theoretical analysis is provided on why nonreciprocal photon transduction enhances inter-atomic excitation transport efficiency. Here, we investigate entanglement mediated by DC current induced nonreciprocal graphene plasmon polaritons. Since nonreciprocal systems have the potential for unidirectional (one-way) beam-like wave propagation, i.e., the ability to efficiently transport photons from one emitter to another, they are ideal for the enhancement, control, and preservation of entanglement [10]. The most traditional way to achieve this is based on the magneto-optical effect, which requires biasing plasma-like materials, e.g., semiconductors, with a static magnetic field. However, due to the need for a strong external magnetic bias, this approach is impractical and typically results in a weak nonreciprocal response at the desired THz and optical frequencies. An alternative way to achieve a nonreciprocal response is to

#473847 https://doi.org/10.1364/OE.473847
Journal © 2023 Received 23 Aug 2022; revised 8 Nov 2022; accepted 30 Nov 2022; published 11 Jan 2023

Optics EXPRESS

bias certain conducting materials (metals, degenerately doped semiconductors, and graphene) with a direct electric current, where a sufficiently strong nonreciprocal effect can be achieved utilizing graphene, given its high electrical conductivity [11–18]. This results in nonreciprocal graphene plasmon polaritons [19–25], which may be a promising candidate to further enhance entanglement mediation.

In this paper, using a quantum master equation and Green's function analysis, we investigate the dynamics of two two-level systems coupled to each other via electric current induced nonreciprocal plasmonic modes of a graphene waveguiding platform. We use concurrence as a measure of entanglement. The theoretical model for this is provided in Sec. 2. In Sec. 3 we establish the nonreciprocal response of the DC current biased graphene, and in Sec. 4 we compare the resulting concurrences to determine whether or not there is an improvement in entanglement enhancement and control. This allows for the further refinement and comparison of the environments that best mediate and maintain entanglement, which is beneficial for the broad applications of entanglement as a quantum resource, including quantum computing [26,27] and quantum cryptography [28].

2. Theoretical model

2.1. Two-qubit entanglement

For a system of two qubits, assuming general (reciprocal or nonreciprocal) media with an external coherent drive (i.e., a laser pump) applied to each qubit, the master equation is ($\rho_s(t) = \rho_s$) [3,5,8,29–32],

$$\begin{aligned}\frac{\partial \rho_s(t)}{\partial t} = &-\frac{i}{\hbar}\left[\mathrm{H_s} + \mathrm{V^{AF}}, \rho_s\right] + \sum_{i=1,2}\frac{\Gamma_{ii}}{2}\left(2\sigma_i\rho_s\sigma_i^\dagger - \sigma_i^\dagger\sigma_i\rho_s - \rho_s\sigma_i^\dagger\sigma_i\right)\\ &+\left(\frac{\Gamma_{21}}{2} + ig_{21}\right)\left(\sigma_2\rho_s\sigma_1^\dagger - \rho_s\sigma_1^\dagger\sigma_2\right) + \left(\frac{\Gamma_{21}}{2} - ig_{21}\right)\left(\sigma_1\rho_s\sigma_2^\dagger - \sigma_2^\dagger\sigma_1\rho_s\right)\\ &+\left(\frac{\Gamma_{12}}{2} + ig_{12}\right)\left(\sigma_1\rho_s\sigma_2^\dagger - \rho_s\sigma_2^\dagger\sigma_1\right) + \left(\frac{\Gamma_{12}}{2} - ig_{12}\right)\left(\sigma_2\rho_s\sigma_1^\dagger - \sigma_1^\dagger\sigma_2\rho_s\right),\end{aligned} \tag{1}$$

where,

$$\mathrm{H}_s = \sum_{i=1,2}\hbar\triangle\omega_i\sigma_i^\dagger\sigma_i, \tag{2}$$

and

$$\mathrm{V^{AF}} = -\hbar\left(\Omega_1 e^{-i\triangle_l t}\sigma_1^\dagger + \Omega_1^* e^{i\triangle_l t}\sigma_1\right) - \hbar\left(\Omega_2 e^{-i\triangle_l t}\sigma_2^\dagger + \Omega_2^* e^{i\triangle_l t}\sigma_2\right). \tag{3}$$

H_s is the Hamiltonian of the decoupled qubits, where $\triangle\omega_i = \omega_0 - \omega_l - \delta_i$, with $\delta_i = g_{ii}$ being the Lamb shift. Since the Lamb shift for optical emitters is typically on the order of a few GHz the effect of the Lamb shift for optical frequencies is small ($\omega_i \sim 10^{12}$ Hz, $\delta_i \sim 10^9$ Hz), therefore the Lamb shift can be ignored, or assumed to be accounted for in the definition of the transition angular frequency ω_0, i.e., $\triangle\omega_i = \omega_0 - \omega_l - \delta_i$ becomes $\triangle\omega_i \approx \omega_0 - \omega_l$. $\mathrm{V^{AF}}$ is the external coherent drive (i.e., a laser pump) applied to each qubit, where $\triangle_l = \omega_0 - \omega_l$, which is the detuning parameter, with ω_l being the laser angular frequency, and $\Omega_i = \frac{(\mathbf{d}\cdot\mathbf{E}_0^i)}{\hbar}$, which is a Rabi frequency. Here the external coherent drive field is treated as a classical number given its large amplitude.

Optics EXPRESS

Assuming $\omega_0 = \omega_l$ and $\Omega_i = \Omega_i^*$, Eq. (1) then becomes

$$\begin{aligned}\frac{\partial \rho_s(t)}{\partial t} &= i\Omega_1\left(\left(\sigma_1^\dagger\rho_s + \sigma_1\rho_s\right) - \left(\rho_s\sigma_1^\dagger + \rho_s\sigma_1\right)\right) + i\Omega_2\left(\left(\sigma_2^\dagger\rho_s + \sigma_2\rho_s\right) - \left(\rho_s\sigma_2^\dagger + \rho_s\sigma_2\right)\right)\\ &+ \frac{\Gamma_{11}}{2}\left(2\sigma_1\rho_s\sigma_1^\dagger - \sigma_1^\dagger\sigma_1\rho_s - \rho_s\sigma_1^\dagger\sigma_1\right) + \frac{\Gamma_{22}}{2}\left(2\sigma_2\rho_s\sigma_2^\dagger - \sigma_2^\dagger\sigma_2\rho_s - \rho_s\sigma_2^\dagger\sigma_2\right)\\ &+ \left(\frac{\Gamma_{21}}{2} + ig_{21}\right)\left(\sigma_2\rho_s\sigma_1^\dagger - \rho_s\sigma_1^\dagger\sigma_2\right) + \left(\frac{\Gamma_{21}}{2} - ig_{21}\right)\left(\sigma_1\rho_s\sigma_2^\dagger - \sigma_2^\dagger\sigma_1\rho_s\right)\\ &+ \left(\frac{\Gamma_{12}}{2} + ig_{12}\right)\left(\sigma_1\rho_s\sigma_2^\dagger - \rho_s\sigma_2^\dagger\sigma_1\right) + \left(\frac{\Gamma_{12}}{2} - ig_{12}\right)\left(\sigma_2\rho_s\sigma_1^\dagger - \sigma_1^\dagger\sigma_2\rho_s\right),\end{aligned} \tag{4}$$

where

$$\Gamma_{\alpha\beta}(\omega_0) = \frac{2}{\varepsilon_0\hbar}\mathrm{Im}\left\{\mathbf{d}\cdot\underline{\mathbf{G}}(\mathbf{r}_\alpha,\mathbf{r}_\beta,\omega_0)\cdot\mathbf{d}\right\}, \tag{5}$$

$$g_{\alpha\beta}(\omega_0) = \frac{1}{\varepsilon_0\hbar}\mathrm{Re}\left\{\mathbf{d}\cdot\underline{\mathbf{G}}(\mathbf{r}_\alpha,\mathbf{r}_\beta,\omega_0)\cdot\mathbf{d}\right\}. \tag{6}$$

In Eqs. (5) and (6), $\mathbf{d}$ is the atom (qubit) transition dipole moment, $\Gamma_{\alpha\alpha}$ and $\Gamma_{\alpha\beta}$ ($\alpha \neq \beta$) are the dissipative decay rates of qubit α due to its interaction with the environment and its interaction with qubit β through the environment, $g_{\alpha\beta}$ ($\alpha \neq \beta$) is the qubits' transition frequency shift induced by dipole-dipole coupling, and $\underline{\mathbf{G}}(\mathbf{r}_\alpha, \mathbf{r}_\beta, \omega_0)$ is the Green's tensor representing the environment. Note that $\Gamma_{12} = \Gamma_{21}$ and $g_{12} = g_{21}$ for the reciprocal case, and for identical emitters (qubits), which we assume in this work, $\Gamma_{11} = \Gamma_{22}$.

2.2. Green's function

We solve for the Green's tensor that satisfies [3,29–32],

$$\nabla\times\nabla\times\underline{\mathbf{G}}(\mathbf{r},\mathbf{r}',\omega) - k_0^2\mu_r(\mathbf{r},\omega)\varepsilon_r(\mathbf{r},\omega)\underline{\mathbf{G}}(\mathbf{r},\mathbf{r}',\omega) = k_0^2\underline{\mathbf{I}}\delta(\mathbf{r}-\mathbf{r}'), \tag{7}$$

where $\mathbf{r}, \mathbf{r}'$ are the observation and source point vectors, respectively, $k_0 = \frac{\omega}{c} = \omega\sqrt{\mu_0\varepsilon_0}$ is the vacuum wavenumber, ω is the angular frequency, c is the speed of light in vacuum, $\mu_r(\mathbf{r},\omega)$ is the relative permeability, $\varepsilon_r(\mathbf{r},\omega)$ is the relative permittivity, and $\underline{\mathbf{I}}$ is the unit 3-by-3 tensor. We assume that we are working with non-magnetic materials so we set $\mu_r(\mathbf{r},\omega) = 1$. Additionally, throughout this work we assume time-harmonic fields with time variations of the form $e^{-i\omega t}$.

The model for the case of a single interface (in this case a sheet of graphene modeled as an infinitesimally thin local two-sided surface characterized by a surface conductivity σ) between two different materials (μ_2, ε_2 for z>0, μ_1, ε_1 for z<0) [33] is seen in Fig. 1. We assume the interface is an infinite plane (in this case an infinite sheet of graphene), where we also assume the source point and the observation point are both above the interface, i.e., in region 2. Additionally, we assume that the two atoms (qubits) have a dipole moment of $\mathbf{d} = \hat{\mathbf{z}}d$, i.e., they are polarized perpendicular to the interface, with qubit one (QB1) at (x', y', z'), and qubit two (QB2) at (x, y, z), so that $\mathbf{R} = \mathbf{r}-\mathbf{r}' = (x-x')\hat{\mathbf{x}}+(y-y')\hat{\mathbf{y}}+(z-z')\hat{\mathbf{z}}$, where $R = |\mathbf{R}| = \sqrt{(x-x')^2+(y-y')^2+(z-z')^2}$, and with $\rho = \sqrt{(x-x')^2+(y-y')^2}$, then, $R = |\mathbf{R}| = \sqrt{\rho^2+(z-z')^2}$. We also assume that the qubits are at the same height, i.e., $z = z'$, which leads to $R = \rho$, and that QB1 is always located at the origin ($x' = 0$, $y' = 0$), i.e., at the center of the graphene sheet (x-y plane). We can apply a DC voltage to the graphene sheet as shown in Fig. 1, where a drift velocity will be induced by the DC current.

Optics EXPRESS

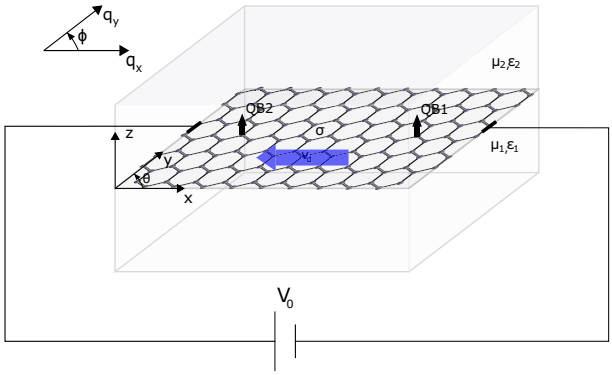

Fig. 1. Model for the case of a single interface (in this case an infinite sheet of graphene modeled as an infinitesimally thin local two-sided surface characterized by a surface conductivity σ) between two different materials (μ_2, ε_2 for z>0, μ_1, ε_1 for z<0). The graphene sheet is biased with a DC voltage, where the blue arrow represents the drift velocity induced by the DC current.

For this geometry we can express the solution to Eq. (7) as

$$\underline{\mathbf{G}}(\mathbf{r},\mathbf{r}',\omega) = \left[\underline{\mathbf{I}}k_2^2 + \nabla\nabla\cdot\right]\left\{\underline{\mathbf{g}}^p(\mathbf{r},\mathbf{r}',\omega) + \underline{\mathbf{g}}^s(\mathbf{r},\mathbf{r}',\omega)\right\}, \tag{8}$$

where we are solving for the Green's function in region 2, therefore we use $k_2 = \omega\sqrt{\mu_2\varepsilon_2}$ as the wavenumber. Here, $\underline{\mathbf{g}}^p(\mathbf{r},\mathbf{r}',\omega)$ is the principle Green's function (the solution to Eq. (7) when $\varepsilon_r(\mathbf{r},\omega) = \varepsilon_{r2}(\mathbf{r},\omega)$, i.e., the Green's function for a homogeneous medium (a single region (region 2) with no interface)), and $\underline{\mathbf{g}}^s(\mathbf{r},\mathbf{r}',\omega)$ is the scattered Green's function (the solution to Eq. (7) accounting for the field scattered from the media (the interface and the regions)). With $\mathbf{d} = \hat{\mathbf{z}}d$, then $\mathbf{d}\cdot\underline{\mathbf{G}}(\mathbf{r},\mathbf{r}')\cdot\mathbf{d}$, which is ultimately what we will need in Eqs. (5) and (6), becomes (using the expression for $\underline{\mathbf{G}}(\mathbf{r},\mathbf{r}',\omega)$ from Eq. (8))

$$\mathbf{d}\cdot\underline{\mathbf{G}}(\mathbf{r},\mathbf{r}')\cdot\mathbf{d} = d^2G_{zz} = d^2\left[k_2^2\left(g_{zz}^p + g_{zz}^s\right) + \frac{\partial^2}{\partial z^2}\left(g_{zz}^p + g_{zz}^s\right)\right], \tag{9}$$

where

$$g_{zz}^p = \frac{e^{ik_2R}}{4\pi R} = \frac{e^{ik_2\sqrt{\rho^2+(z-z')^2}}}{4\pi\sqrt{\rho^2+(z-z')^2}}, \tag{10}$$

and [33]

$$g_{zz}^s = \frac{1}{(2\pi)^2}\int_0^\infty\int_{-\pi}^{\pi} R_n e^{-p_2(z+z')}\frac{e^{iq\rho\cos(\phi-\theta)}}{2p_2}qd\phi dq, \tag{11}$$

where,

$$R_n = \frac{\frac{\varepsilon_1}{\varepsilon_2}p_2 - p_1 + \frac{\sigma_d p_2 p_1}{-i\omega\varepsilon_2}}{\frac{\varepsilon_1}{\varepsilon_2}p_2 + p_1 + \frac{\sigma_d p_2 p_1}{-i\omega\varepsilon_2}} = \frac{N^E}{Z^E}, \tag{12}$$

$\varepsilon_1 = \varepsilon_0\varepsilon_{r1}$, $\varepsilon_2 = \varepsilon_0\varepsilon_{r2}$, $p_1 = \sqrt{q^2 - k_1^2}$, and $p_2 = \sqrt{q^2 - k_2^2}$. Note that we can also express $e^{iq\rho\cos(\phi-\theta)}$ in Eq. (11) as $e^{iq(\cos(\phi)x+\sin(\phi)y)}$, where in both cases ϕ is defined as the angle in the momentum coordinate space shown in Fig. 1. We will define a nonlocal surface conductivity σ_d

Optics EXPRESS

in Sec. 3.1, where we will see that for a drift velocity $v_d = 0$, $\sigma_d = \sigma$, defined in Sec. 2.3. In that case, $\sigma_d \to \sigma$, we can use a Bessel function identity for the ϕ integral for g^s_{zz}, leading to

$$g^s_{zz} = \frac{1}{2\pi}\int_0^\infty R_n(\sigma_d \to \sigma) e^{-p_2(z+z')} \frac{J_0(q\rho)}{2p_2} q dq. \tag{13}$$

To obtain the electric field from the Green's function we use

$$E_z = \frac{\mu_{r2} G_{zz}}{-i\omega\varepsilon_0} = \frac{G_{zz}}{-i\omega\varepsilon_0}. \tag{14}$$

2.3. Local surface conductivity for graphene

We define the local surface conductivity σ for graphene as (in the low-temperature limit) [34]

$$\sigma(\omega) = \frac{ie^2\mu_c}{\pi\hbar^2(\omega + i\Gamma)} + \frac{e^2}{4\hbar}\left[\Theta(\hbar\omega - 2\mu_c) + \frac{i}{\pi}\ln\left|\frac{\hbar\omega - 2\mu_c}{\hbar\omega + 2\mu_c}\right|\right], \tag{15}$$

where $\Theta(x)$ is the Heaviside function and e is the charge of an electron.

In Eq. (15), μ_c is the chemical potential (Fermi energy) and Γ is the phenomenological intraband scattering rate, where $\Gamma = \frac{1}{\tau}$ (τ is the intraband scattering time). In this work we use [23] $\mu_c = 0.1$ eV and $\tau = 0.35$ ps. Then, using these values, we obtain the plot inset in Fig. 2(a) for the local surface conductivity $\sigma(\omega)$ for graphene. Additionally, since we are only interested in TM surface modes we need to ensure that we are working at a frequency where the imaginary part of $\sigma(\omega)$ (or the conductivity with the Doppler-shifted frequency used in the σ_d expression in Sec. 3.1) is positive [34].

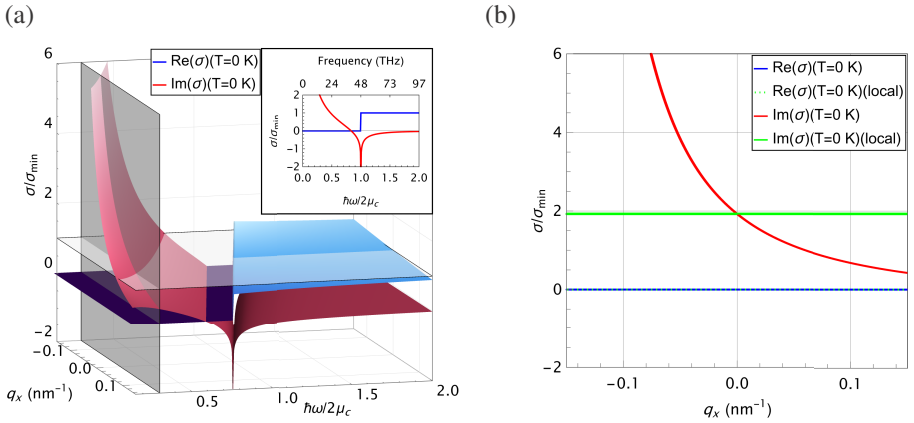

Fig. 2. Nonlocal surface conductivity $\sigma_d(v_d, q_x, \omega)$ for graphene (in the low-temperature limit), where $\mu_c = 0.1$ eV, $\tau = 0.35$ ps, and $\sigma_{\min} = \frac{(\pi e^2)}{(2h)}$ (h is Planck's constant): (a) nonlocal conductivity for $v_d = \frac{-v_F}{2}$, with inset of local surface conductivity $\sigma(\omega)$, and (b) nonlocal conductivity for $v_d = \frac{-v_F}{2}$ at 15 THz (on the plane at 15 THz in (a)), where the local conductivity at 15 THz is also included for reference. A plane is included in (a) at $\frac{\sigma}{\sigma_{\min}} = 1$ for reference to better see changes to $\frac{\sigma}{\sigma_{\min}}$ as q_x changes.

2.4. Concurrence

We use the expression for concurrence in the general case (reciprocal or nonreciprocal) [8,35],

$$C(t) = \max\left(0, \sqrt{u_1} - \sqrt{u_2} - \sqrt{u_3} - \sqrt{u_4}\right), \tag{16}$$

as a measure of the amount of entanglement between the qubits (varies from 0 (unentangled) to 1 (completely entangled), where u_i are the eigenvalues, arranged in descending order, of the matrix

Optics EXPRESS

$\rho(t)\rho^{y}(t)$, where $\rho^{y}(t) = \sigma_{y_1} \otimes \sigma_{y_2}\rho^{*}(t)\sigma_{y_1} \otimes \sigma_{y_2}$ is the spin-flip density matrix with σ_{y_i} being the Pauli matrix, $\sigma_{y_i} = \begin{bmatrix} 0 & -i \\ i & 0 \end{bmatrix}$, in the spin-1/2 basis. Expressing σ_{y_i} in terms of the operator basis we are using, the atomic transition operators, $\sigma_i^{+} = \sigma_i^{\dagger} = |e_i\rangle\langle g_i|$, $\sigma_i^{-} = \sigma_i = |g_i\rangle\langle e_i|$, where we have defined $|g_i\rangle = \begin{bmatrix} 1 \\ 0 \end{bmatrix}$, $|e_i\rangle = \begin{bmatrix} 0 \\ 1 \end{bmatrix}$, we have $\sigma_{y_i} = i\left(\sigma_i^{\dagger} - \sigma_i\right) = i\left(|e_i\rangle\langle g_i| - |g_i\rangle\langle e_i|\right) = \begin{bmatrix} 0 & -i \\ i & 0 \end{bmatrix}$. We also solve for $\rho(t)$ (solve Eq. (4)) in that operator basis and the state basis of $|1\rangle = |g_1\rangle|g_2\rangle$, $|2\rangle = |e_1\rangle|e_2\rangle$, $|3\rangle = |g_1\rangle|e_2\rangle$, and $|4\rangle = |e_1\rangle|g_2\rangle$, where we assume that the initial state of the system is $|\Psi(0)\rangle = |e_1\rangle|g_2\rangle$, i.e., only atom (qubit) one is in the excited state.

3. DC current induced nonreciprocal graphene plasmon polaritons

If we bias the graphene sheet as shown in Fig. 1, we will induce a drift current (drift velocity) on the graphene surface. In the presence of this drift the local surface conductivity for the graphene becomes nonlocal [23–25]. This results in nonreciprocal graphene plasmon polaritons.

3.1. Nonlocal surface conductivity for DC biased graphene

We now define the nonlocal surface conductivity σ_d for DC biased graphene as [23–25]

$$\sigma_d(v_d, q_x, \omega) = \frac{\omega}{\omega - q_x v_d}\sigma(\omega - q_x v_d) = \frac{\omega}{\omega - |q|\cos(\phi)v_d}\sigma(\omega - |q|\cos(\phi)v_d), \tag{17}$$

where v_d is the drift velocity and q_x is the wavenumber in the momentum space along the x-direction on the graphene surface, where we have assumed that the velocity distribution (e.g., Maxwell-Boltzmann) is such that $v_d \approx v_x \gg v_y$. The resulting nonreciprocal graphene plasmon polaritons become more unidirectional for higher drift velocities, where, for graphene, given its high electrical conductivity [11–18], drift velocities on the order of $v_F \approx \frac{c}{300}$ (v_F being the Fermi velocity) are possible [23].

A plot for the nonlocal surface conductivity for graphene (in the low-temperature limit) for $v_d = \frac{-v_F}{2}$ is provided in Fig. 2, where we can see that the conductivity is nonreciprocal with respect to q_x (larger conductivity in the direction of the drift velocity ($-q_x$-direction)), e.g., see Fig. 2(b), which is the nonlocal conductivity at 15 THz. In other words, the conductivity is tilted along the q_x-axis; smaller in the $+q_x$-direction, becoming larger in the $-q_x$-direction (the direction of the drift velocity). This is commensurate with the nonreciprocal response for the SPPs, where the smaller nonlocal Im (σ) values in the $+q_x$-direction are not sufficient for a strong SPP response [36].

3.2. Dispersion

The dispersion relation for the TM surface waves (the SPPs) supported by the graphene sheet is obtained by setting the denominator, Z^E, in Eq. (12) equal to zero, which results in

$$Z^E = \frac{\varepsilon_1}{\varepsilon_2}p_2 + p_1 + \frac{\sigma_d p_2 p_1}{-i\omega\varepsilon_2} = 0. \tag{18}$$

Then to determine the dispersion we obtain the resulting solution of Eq. (18). Note that throughout this work, when obtaining the results pertaining to the Green's function values (and the corresponding results) the applicable configuration is the graphene sheet embedded in SiO_2, i.e., the relative permittivity in both regions (region 1 and region 2) is $\varepsilon_{r1} = \varepsilon_{r2} = 4$.

Optics EXPRESS

The dispersion for different drift velocity values is shown in Fig. 3, where we can see that for no drift velocity the dispersion is reciprocal for all frequencies, however, for even a small amount of drift velocity there is a nonreciprocal response. For the larger drift velocity values propagation becomes unidirectional (in the direction of the drift velocity), where the SPPs only propagate in one direction above certain frequencies, starting at fairly low THz frequencies for the larger drift velocity values.

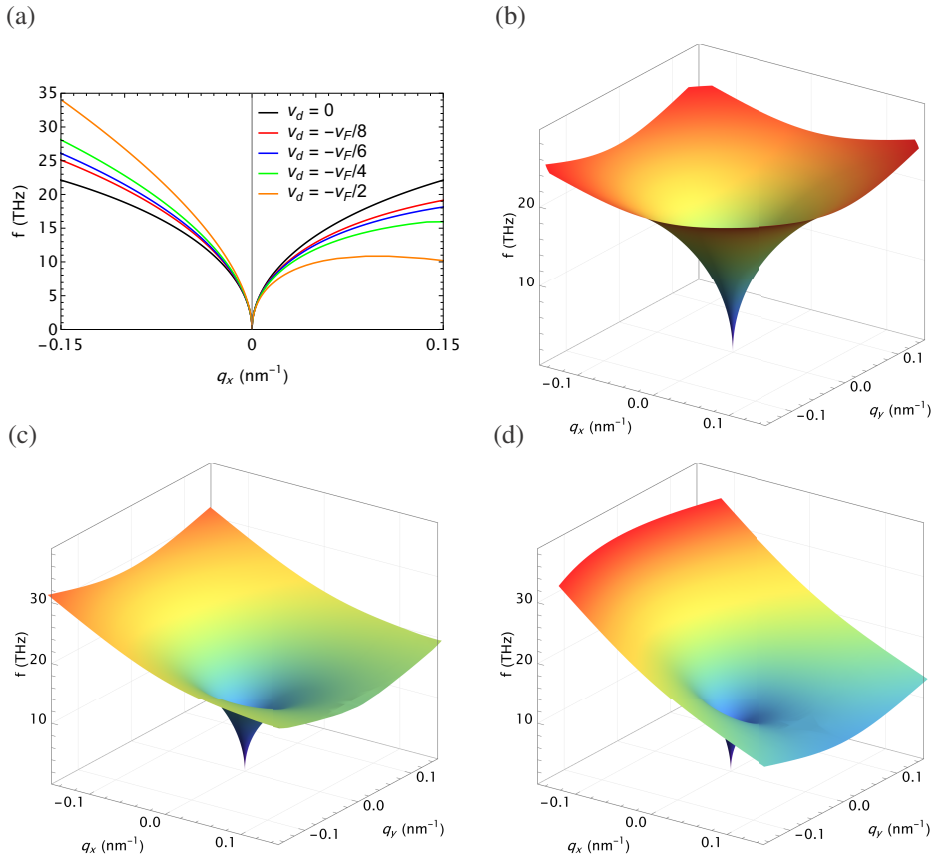

Fig. 3. Dispersion for TM surface waves supported by the graphene sheet for (a) different drift velocity values, (b) graphene reciprocal (R) ($v_d = 0$), (c) graphene nonreciprocal (NR) for $v_d = \frac{-v_F}{4}$, and (d) graphene NR for $v_d = \frac{-v_F}{2}$.

We can also see the effect of the source height on the SPP dispersion by looking at the magnitude of the Green's function integrand for the Sommerfeld integrals at an equi-frequency contour (EFC) at 15 THz. From the plots in Fig. 4 we can see that the intensity of the SPPs (the poles) in the Green's function integrand varies along the EFC as the source height changes; different parts of the EFC become dominant and contribute more as the source height changes.

Throughout this work the qubit separation distances and source (observation) heights are normalized to wavelength. Given the disparity between the wavelengths (at 15 THz the vacuum wavelength is approx. 117 times larger than the SPP wavelengths), we normalize to each respective wavelength, i.e., the qubit separation distances and source (observation) heights are with respect to the 'electrical lengths.' The normalization wavelengths used for vacuum, graphene reciprocal (R), graphene nonreciprocal (NR) for $v_d = \frac{-v_F}{2}$, and graphene nonreciprocal (NR) for $v_d = \frac{-v_F}{4}$ are $\lambda_0 \approx 19.986\ \mu$m, $\lambda_{pr} \approx 0.106\ \mu$m, $\lambda_{pnr1} \approx 0.171\ \mu$m, and $\lambda_{pnr2} \approx 0.137\ \mu$m, respectively.

Optics EXPRESS

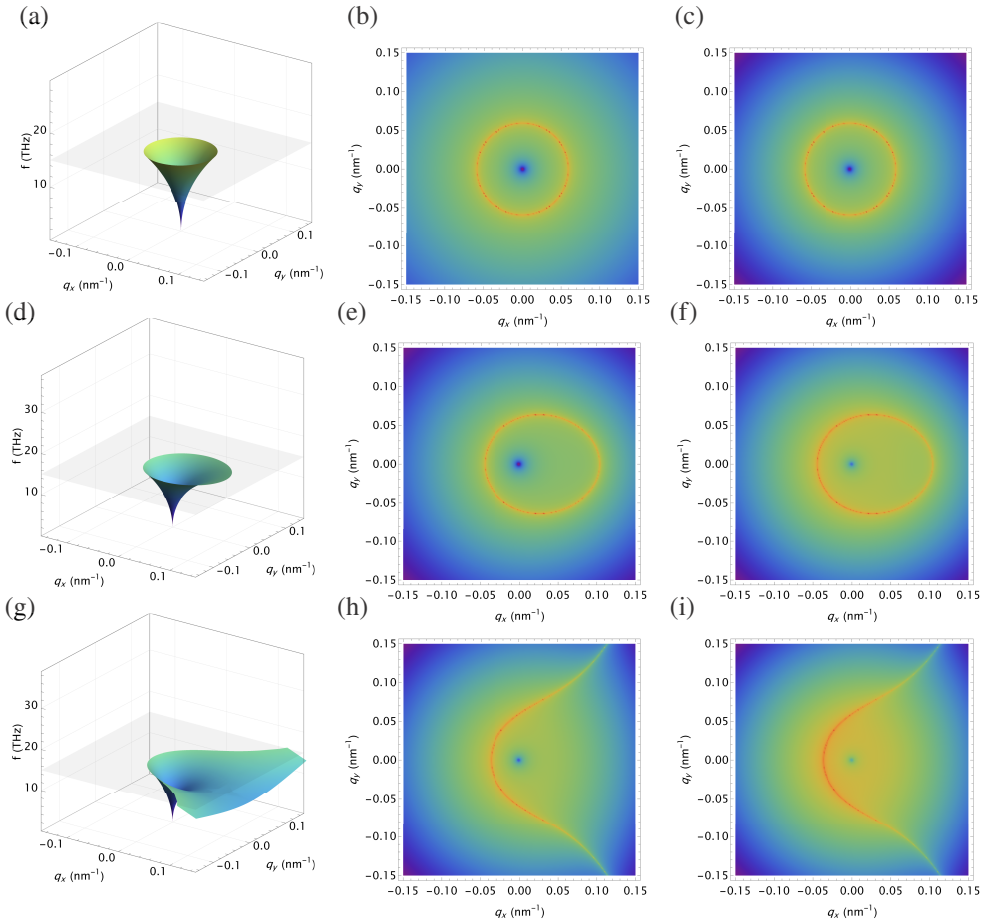

Fig. 4. Effect of the source height on the dispersion for TM surface waves (the SPPs) supported by the graphene sheet: (a) graphene reciprocal (R) ($v_d = 0$) with cut-plane at 15 THz, (b) graphene R ($\lambda = \lambda_{pr}$) with $z = z' = \frac{\lambda}{4}$, (c) graphene R ($\lambda = \lambda_{pr}$) with $z = z' = \frac{\lambda}{3}$, (d) graphene nonreciprocal (NR) for $v_d = \frac{-v_F}{4}$ with cut-plane at 15 THz, (e) graphene NR ($\lambda = \lambda_{pnr2}$) for $v_d = \frac{-v_F}{4}$ with $z = z' = \frac{\lambda}{4}$, (f) graphene NR ($\lambda = \lambda_{pnr2}$) for $v_d = \frac{-v_F}{4}$ with $z = z' = \frac{\lambda}{3}$, (g) graphene NR for $v_d = \frac{-v_F}{2}$ with cut-plane at 15 THz, (h) graphene NR ($\lambda = \lambda_{pnr1}$) for $v_d = \frac{-v_F}{2}$ with $z = z' = \frac{\lambda}{4}$, (i) graphene NR ($\lambda = \lambda_{pnr1}$) for $v_d = \frac{-v_F}{2}$ with $z = z' = \frac{\lambda}{3}$, where the magnitude of the Green's function integrand is plotted (in arb. units) for (b), (c), (e), (f), (h), and (i).

Optics EXPRESS

For no drift velocity the dispersion is reciprocal, and the SPPs (the poles) contribute uniformly to the Green's function integrand along the EFC resulting in the SPP propagation being reciprocal. For nonzero drift velocities the dispersion is nonreciprocal, and the SPPs (the poles) contribute nonuniformly, where there are more poles contributing at different parts of the EFC, which affects the shape and direction of the SPPs propagating on the graphene sheet.

For shorter source heights the SPPs at the extents of the EFC contribute; the shape and direction of the SPP propagation is commensurate. Finally, for larger source heights the SPPs at the extents of the EFC contribute less, and those towards the center are more dominant; the shape and direction of the SPP propagation is more focused in the direction of the drift velocity.

3.3. Electric field

The photon model described here is fully (macroscopically) quantum, although the Green's function provides the classical electric field, which is useful to envision the surface plasmons. In order to see the wave propagation for the reciprocal and nonreciprocal cases we plot the classical electric field, where we can also see the effect of the source height on the electric field response. We obtain the electric field values from the Green's function values using Eq. (14) (all results are for the frequency set to 15 THz). The corresponding plots are in Figs. 5, 6, and 7.

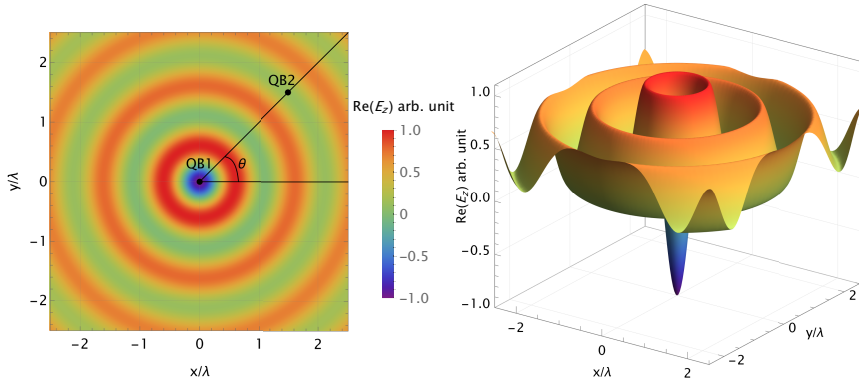

Fig. 5. Electric field wave propagation for graphene R ($v_d = 0$), ($\lambda = \lambda_{pr}$), for $z = z' = \frac{\lambda}{3}$; the plot for $z = z' = \frac{\lambda}{4}$ (not provided) is similar.

For graphene R the wave propagation is the same in all directions, as expected. In the case of graphene NR the wave propagation becomes unidirectional for larger drift velocity values, in the direction of the drift velocity. We also see that for larger source heights, that are still in the vicinity of the interface, the shape and direction of the propagation is more focused in the direction of the drift velocity, which is commensurate with what was observed for the effect of the source height on the dispersion for the SPPs. However, if the source height becomes too large, i.e., too far from the interface, the source will not couple with the interface enough to result in a strong nonreciprocal SPP response.

Optics EXPRESS

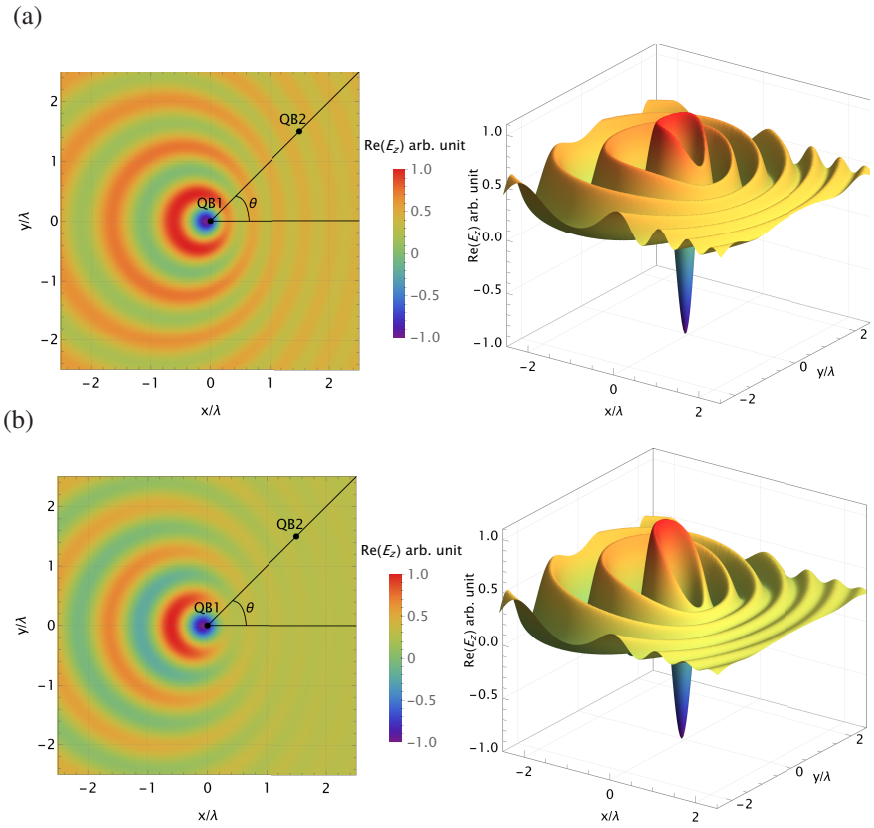

Fig. 6. Electric field wave propagation for graphene NR ($\lambda = \lambda_{pnr2}$) for $v_d = \frac{-v_F}{4}$: (a) $z = z' = \frac{\lambda}{4}$ and (b) $z = z' = \frac{\lambda}{3}$.

Optics EXPRESS

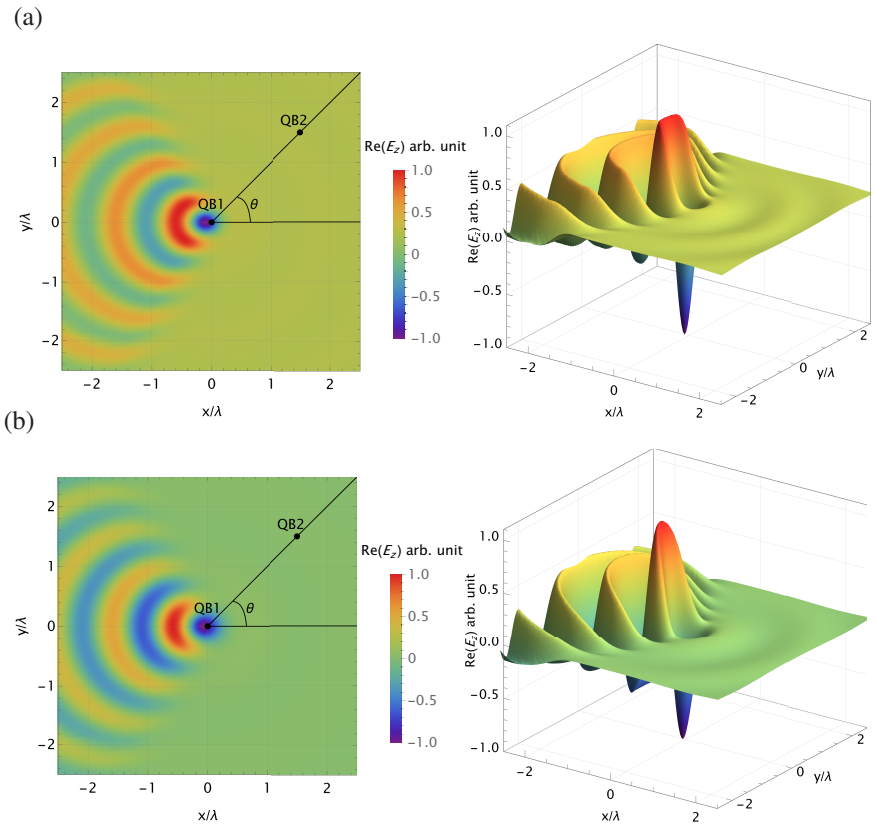

Fig. 7. Electric field wave propagation for graphene NR ($\lambda = \lambda_{pnr1}$) for $v_d = \frac{-v_F}{2}$: (a) $z = z' = \frac{\lambda}{4}$ and (b) $z = z' = \frac{\lambda}{3}$.

Optics EXPRESS

4. Results

To determine which direction concurrence is maximized we plot concurrence versus angle, where we consider $0° \leq \theta \leq 180°$ only given the symmetry about the y-axis. We position the qubits in the configuration defined in Figs. 5, 6, and 7, where we set the qubit separation distance $\rho = 2\lambda$ and sweep θ from 0° to 180°, determining the maximum concurrence versus time at each angle, i.e., $C(\theta) = \max_t (C(\rho, \theta, t))$. As seen in Fig. 8(a), there is good control over concurrence (entanglement) as a function of angle for the nonreciprocal (NR) cases. Additionally, the concurrence is higher for larger drift velocities, i.e., for higher directionality of the field. Also, in the NR case, the concurrence is higher, at the maximum angle, for the larger source height. Finally, there is good enhancement of entanglement for the NR case, at the maximum angle, over the reciprocal (R) case and vacuum.

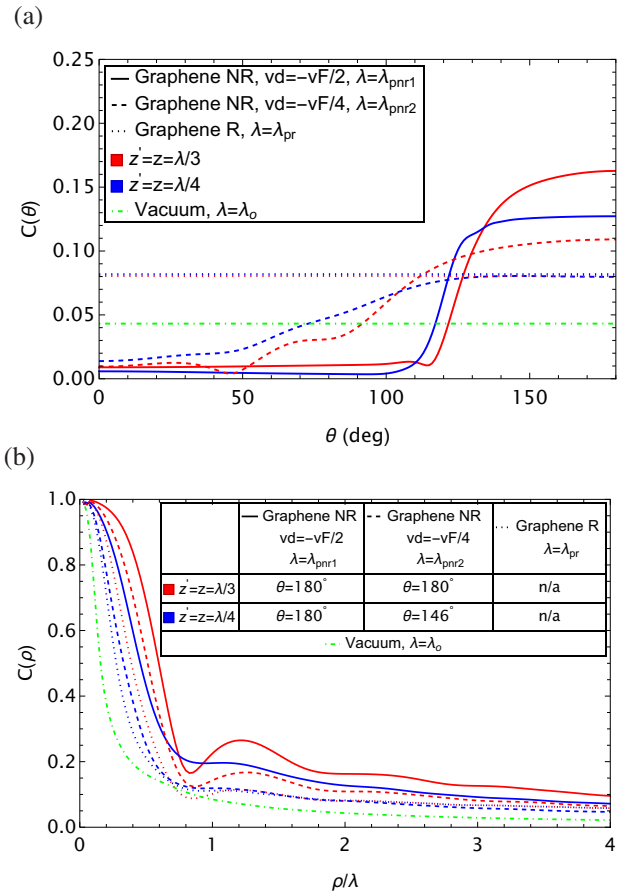

Fig. 8. Concurrence versus angle and qubit separation distance for the qubit position configuration defined in Figs. 5, 6, and 7, where we consider $0° \leq \theta \leq 180°$ only given the symmetry about the y-axis: (a) concurrence versus angle, where we obtained the maximum $C(t)$, at a qubit separation distance of $\rho = 2\lambda$, for each angle, i.e., $C(\theta) = \max_t (C(\rho, \theta, t))$, and (b) concurrence versus qubit separation distance, where we obtained the maximum $C(t)$, at the maximum angle determined in (a), where applicable, for each qubit separation distance ρ, i.e., $C(\rho) = \max_t (C(\rho, \theta, t))$. In all cases the plots were done for two different observation and source heights, $z = z' = \frac{\lambda}{4}$ and $z = z' = \frac{\lambda}{3}$.

Optics EXPRESS

We then plot concurrence as a function of ρ, at the applicable maximum angle, to see how the concurrences compare to each other with respect to the qubit separation distance; determining the maximum concurrence versus time at each ρ value, i.e., $C(\rho) = \max_t (C(\rho, \theta, t))$. We can see from Fig. 8(b) that the entanglement for the NR case is better than the R case, and vacuum, for fairly large qubit separation distances.

We also plot concurrence versus time (for the transient case, (the pump intensities $\Omega_1 = \Omega_2 = 0$)), at the maximum angle and a qubit separation distance of $\rho = 2\lambda$, i.e., $C(t) = \max_\theta (C(\rho, \theta, t))$, to compare the concurrences. As seen in Fig. 9(a), there is good enhancement for the NR case over the R case and vacuum, which is the case for larger qubit separation distances as well.

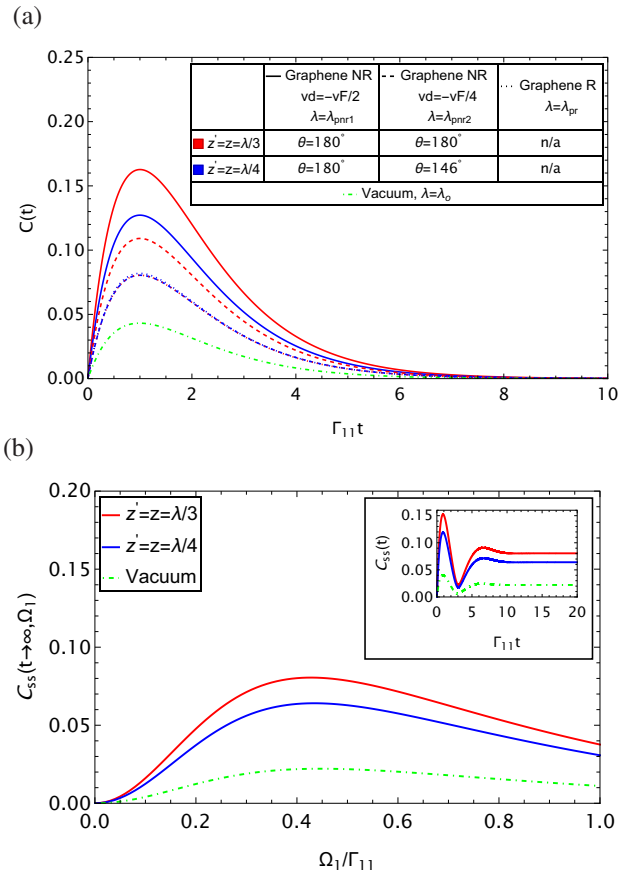

Fig. 9. Concurrence versus time, where we look at $C(t)$ for the maximum angle determined in Fig. 8(a): (a) concurrence versus transient time (the pump intensities $\Omega_1 = \Omega_2 = 0$)), $C(t)$, at the maximum angle and a qubit separation distance of $\rho = 2\lambda$, i.e., $C(t) = \max_\theta (C(\rho, \theta, t))$, and (b) steady state concurrence at $t \to \infty$, $C_{ss}(t \to \infty)$, versus Ω_1, for the maximum angle and a qubit separation distance of $\rho = 2\lambda$, i.e., $C_{ss}(t \to \infty, \Omega_1) = \max_\theta (C(\rho, \theta, t \to \infty, \Omega_1))$, where the laser pump intensity at QB2 is set to zero ($\Omega_2 = 0$). The inset in (b) is $C_{ss}(t)$ for the Ω_1 value where $C_{ss}(t \to \infty)$ is maximum ($\Omega_1 = 0.45\Gamma_{11}$ for the vacuum plot and $\Omega_1 = 0.43\Gamma_{11}$ for the other plots), where ($\Omega_2 = 0$). In (b) the plots were done for the cases of $v_d = \frac{-v_F}{2}$ and vacuum, and in both (a) and (b), the plots for $v_d = \frac{-v_F}{2}$ were done for two different observation and source heights, $z = z' = \frac{\lambda}{4}$ and $z = z' = \frac{\lambda}{3}$.

In order to maintain the entanglement an external coherent drive (i.e., a laser pump) is implemented at each qubit, where different pumping profiles can be applied. We apply the laser

Optics EXPRESS

pump at QB1 only, without applying one at QB2 (the laser pump intensity at QB2 is set to zero ($\Omega_2 = 0$)). We determine the maximum steady state concurrence at $t \to \infty$, $C_{ss}(t \to \infty)$, by plotting $C_{ss}(t \to \infty)$ versus Ω_1, for the maximum angle and a qubit separation distance of $\rho = 2\lambda$, i.e., $C_{ss}(t \to \infty, \Omega_1) = \max_\theta (C(\rho, \theta, t \to \infty, \Omega_1))$. We then plot $C_{ss}(t)$ for the Ω_1 value where $C_{ss}(t \to \infty)$ is maximum (see the inset in Fig. 9(b)). All of the plots in Fig. 9(b) are done for the cases of $v_d = \frac{-v_F}{2}$ and vacuum. As seen in Fig. 9(b), $C_{ss}(t \to \infty, \Omega_1)$ is small for low and high values for Ω_1, and is maximum for values that are close to the middle of that range.

Since it was shown that there is good control over concurrence (entanglement) as a function of angle, we can use this configuration to control entanglement (controlling which qubits are entangled by means of changing the polarity of the DC bias, i.e., the direction of the drift velocity). As seen in Fig. 10(a) (note that for the proposed system configuration only pairwise entanglement needs to be considered since coupling with the third qubit is so weak that we can assume it doesn't exist), for the graphene biased such that $v_d = \frac{-v_F}{2}$, QB1 is entangled with QB2, however, QB1 is not entangled with QB3. Now, if the graphene is biased such that $v_d = \frac{v_F}{2}$, as seen in Fig. 10(b), then QB1 is not entangled with QB2, however, QB1 is entangled with QB3.

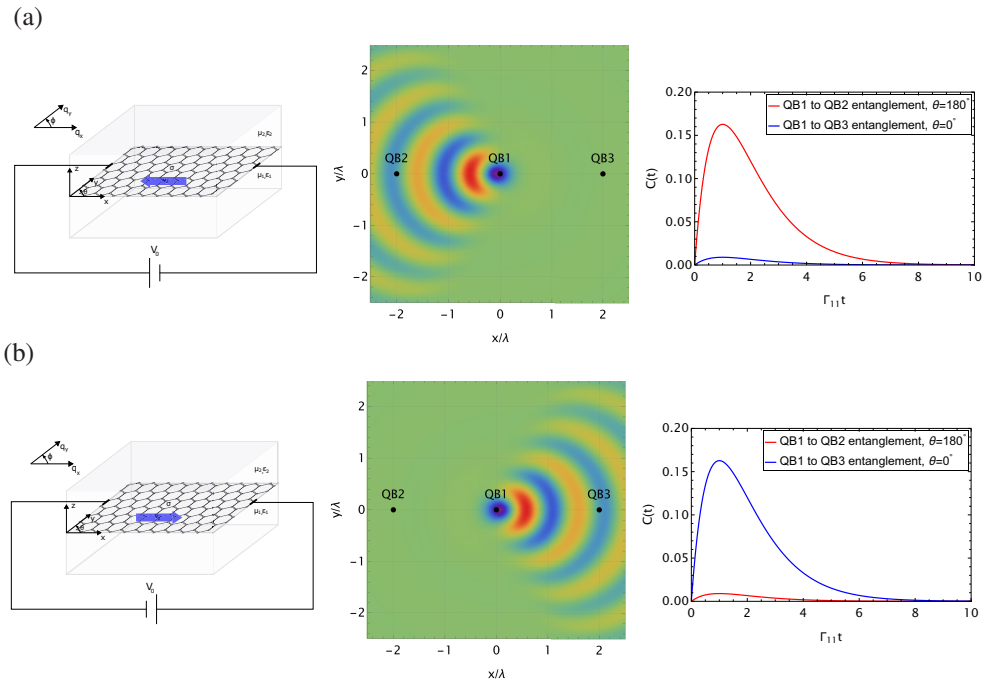

Fig. 10. Configuration for use of the proposed system as a means for entanglement control (note that for the proposed system configuration only pairwise entanglement needs to be considered since coupling with the third qubit is so weak that we can assume it doesn't exist): (a) graphene biased such that $v_d = \frac{-v_F}{2}$ and (b) graphene biased such that $v_d = \frac{v_F}{2}$. In all cases, the observation and source heights are $z = z' = \frac{\lambda}{3}$ and the qubit separation distances are $\rho = 2\lambda$.

5. Conclusion

We investigated DC current induced nonreciprocal graphene plasmon polaritons as a candidate for entanglement mediation for enhancement over vacuum. We used concurrence as a measure of entanglement. It was shown that biasing the graphene sheet with a DC current induces

Optics EXPRESS

a nonreciprocal response with highly directed energy, which can be used for entanglement enhancement and control. We have shown that there was good entanglement enhancement over vacuum and that the proposed configuration can be used to control which qubits are entangled by changing the polarity of the DC bias.

Funding. NATO Science for Peace and Security project (NATO.SPS.MYP.G5860).

Disclosures. The authors declare no conflicts of interest.

Data availability. Data underlying the results presented in this paper are not publicly available at this time but may be obtained from the authors upon reasonable request.

References

1. A. Gonzalez-Tudela, D. Martin-Cano, E. Moreno, L. Martin-Moreno, C. Tejedor, and F. J. Garcia-Vidal, "Entanglement of two qubits mediated by one-dimensional plasmonic waveguides," Phys. Rev. Lett. **106**(2), 020501 (2011).
2. D. Martín-Cano, A. González-Tudela, L. Martín-Moreno, F. J. García-Vidal, C. Tejedor, and E. Moreno, "Dissipation-driven generation of two-qubit entanglement mediated by plasmonic waveguides," Phys. Rev. B **84**(23), 235306 (2011).
3. S. A. H. Gangaraj, A. Nemilentsau, G. W. Hanson, and S. Hughes, "Transient and steady-state entanglement mediated by three-dimensional plasmonic waveguides," Opt. Express **23**(17), 22330–22346 (2015).
4. Z. Wang, Y. D. Chong, J. D. Joannopoulos, and M. Soljačić, "Reflection-free one-way edge modes in a gyromagnetic photonic crystal," Phys. Rev. Lett. **100**(1), 013905 (2008).
5. S. Y. Buhmann, D. T. Butcher, and S. Scheel, "Macroscopic quantum electrodynamics in nonlocal and nonreciprocal media," New J. Phys. **14**(8), 083034 (2012).
6. M. G. Silveirinha, "Chern invariants for continuous media," Phys. Rev. B **92**(12), 125153 (2015).
7. C. Gonzalez-Ballestero, A. Gonzalez-Tudela, F. J. Garcia-Vidal, and E. Moreno, "Chiral route to spontaneous entanglement generation," Phys. Rev. B **92**(15), 155304 (2015).
8. S. A. H. Gangaraj, G. W. Hanson, and M. Antezza, "Robust entanglement with three-dimensional nonreciprocal photonic topological insulators," Phys. Rev. A **95**(6), 063807 (2017).
9. S. A. H. Gangaraj, L. Ying, F. Monticone, and Z. Yu, "Enhancement of quantum excitation transport by photonic nonreciprocity," arXiv, arXiv:2204.12473v1 [quant-ph] (2022).
10. P. Lodahl, S. Mahmoodian, S. Stobbe, A. Rauschenbeutel, P. Schneeweiss, J. Volz, H. Pichler, and P. Zoller, "Chiral quantum optics," Nature (London) **541**(7638), 473–480 (2017).
11. A. H. C. Neto, F. Guinea, N. M. R. Peres, K. S. Novoselov, and A. K. Geim, "The electronic properties of graphene," Rev. Mod. Phys. **81**(1), 109–162 (2009).
12. R. S. Shishir and D. K. Ferry, "Velocity saturation in intrinsic graphene," J. Phys.: Condens. Matter **21**(34), 344201 (2009).
13. V. E. Dorgan, M.-H. Bae, and E. Pop, "Mobility and saturation velocity in graphene on sio2," Appl. Phys. Lett. **97**(8), 082112 (2010).
14. M. D. Ozdemir, O. Atasever, B. Ozdemir, Z. Yarar, and M. Ozdemir, "A comparative study of transport properties of monolayer graphene and algan-gan heterostructure," AIP Adv. **5**(7), 077101 (2015).
15. H. Ramamoorthy, R. Somphonsane, J. Radice, G. He, C.-P. Kwan, and J. P. Bird, "'Freeing' graphene from its substrate: Observing intrinsic velocity saturation with rapid electrical pulsing," Nano Lett. **16**(1), 399–403 (2016).
16. M. A. Yamoah, W. Yang, E. Pop, and D. Goldhaber-Gordon, "High-velocity saturation in graphene encapsulated by hexagonal boron nitride," ACS Nano **11**(10), 9914–9919 (2017).
17. M. Sabbaghi, H.-W. Lee, and T. Stauber, "Electro-optics of current-carrying graphene," Phys. Rev. B **98**(7), 075424 (2018).
18. M. Sabbaghi, T. Stauber, H.-W. Lee, J. S. Gomez-Diaz, and G. W. Hanson, "In-plane optical phonon modes of current-carrying graphene," Phys. Rev. B **105**(23), 235405 (2022).
19. M. Sabbaghi, H.-W. Lee, T. Stauber, and K. S. Kim, "Drift-induced modifications to the dynamical polarization of graphene," Phys. Rev. B **92**(19), 195429 (2015).
20. B. Van Duppen, A. Tomadin, A. N. Grigorenko, and M. Polini, "Current-induced birefringent absorption and non-reciprocal plasmons in graphene," 2D Mater. **3**(1), 015011 (2016).
21. T. A. Morgado and M. G. Silveirinha, "Negative landau damping in bilayer graphene," Phys. Rev. Lett. **119**(13), 133901 (2017).
22. T. Wenger, G. Viola, J. Kinaret, M. Fogelström, and P. Tassin, "Current-controlled light scattering and asymmetric plasmon propagation in graphene," Phys. Rev. B **97**(8), 085419 (2018).
23. T. A. Morgado and M. G. Silveirinha, "Drift-induced unidirectional graphene plasmons," ACS Photonics **5**(11), 4253–4258 (2018).
24. D. Correas-Serrano and J. S. Gomez-Diaz, "Nonreciprocal and collimated surface plasmons in drift-biased graphene metasurfaces," Phys. Rev. B **100**(8), 081410 (2019).
25. S. A. Hassani Gangaraj and F. Monticone, "Drifting electrons: Nonreciprocal plasmonics and thermal photonics," ACS Photonics **9**(3), 806–819 (2022).

Optics EXPRESS

26. M. A. Nielsen, *Quantum computation and quantum information / Michael A. Nielsen and Isaac L. Chuang*. (Cambridge University, 2000).
27. M. Wilde, *Quantum information theory / Mark M. Wilde, McGill University, Montréal*. (Cambridge University, 2013).
28. A. Acín, L. Masanes, and S. Pironio, "Secure device-independent quantum key distribution with causally independent measurement devices," Nat. Commun. **2**(1), 238 (2011).
29. T. Gruner and D. Welsch, "Green-function approach to the radiation-field quantization for homogeneous and inhomogeneous kramers-kronig dielectrics," Phys. Rev. A **53**(3), 1818–1829 (1996).
30. H. T. Dung, L. Knöll, and D.-G. Welsch, "Three-dimensional quantization of the electromagnetic field in dispersive and absorbing inhomogeneous dielectrics," Phys. Rev. A **57**(5), 3931–3942 (1998).
31. H. T. Dung, L. Knöll, and D.-G. Welsch, "Spontaneous decay in the presence of dispersing and absorbing bodies: General theory and application to a spherical cavity," Phys. Rev. A **62**(5), 053804 (2000).
32. G. Angelatos and S. Hughes, "Entanglement dynamics and mollow nonuplets between two coupled quantum dots in a nanowire photonic-crystal system," Phys. Rev. A **91**(5), 051803 (2015).
33. G. W. Hanson, "Dyadic green's functions and guided surface waves for a surface conductivity model of graphene," J. Appl. Phys. **103**(6), 064302 (2008).
34. G. W. Hanson, S. A. Hassani Gangaraj, C. Lee, D. G. Angelakis, and M. Tame, "Quantum plasmonic excitation in graphene and loss-insensitive propagation," Phys. Rev. A **92**(1), 013828 (2015).
35. W. Wootters, "Entanglement of formation and concurrence," Quantum Inf. & Comput. **1**(1), 27–44 (2001).
36. F. Liang, A. B. Yakovlev, and G. W. Hanson, "Optimum surface plasmon excitation and propagation on conductive two-dimensional materials and thin films," IEEE Trans. Antennas Propag. **63**(4), 1765–1774 (2015).